



Axial crushing of pressurized cylindrical tubes



L.L. Hu ^{a,b,*}, Zh.H. Zeng ^a, T.X. Yu ^c

^a Department of Applied Mechanics & Engineering, School of Engineering, Sun Yat-sen University, Guangzhou 510275, PR China

^b State Key Laboratory for Strength and Vibration of Mechanical Structures, Xi'an 710049, PR China

^c Department of Mechanical & Aerospace Engineering, The Hong Kong University of Science and Technology, Clear Water Bay, Kowloon, Hong Kong

ARTICLE INFO

Article history:

Received 11 November 2015

Received in revised form

22 December 2015

Accepted 7 January 2016

Available online 18 January 2016

Keywords:

Cylindrical tube

Internal pressure

Load-carrying capacity

Axial crushing

ABSTRACT

The crushing response of the pressurized cylindrical tubes under low-speed axial crushing is investigated by both numerical simulations and theoretical analysis. The internal pressure inside the tubes varies in a wide range from 0% to 80% of the tube's yield pressure. Numerical simulations with lower internal pressure are verified by the experiments reported in literatures. It is shown that under axial crushing the tubes with lower internal pressure deform into the mixture of symmetric mode and unsymmetrical mode. With the increase of internal pressure, the tube's deformation under axial crushing is dominated by the symmetric mode. The total load-carrying capacity of the pressurized structure increases with the internal pressure. However, the load-carrying capacity of the tube wall itself decreases with the increase of internal pressure once the pressure is greater than 13% of the yield pressure. This behavior is very different from the foam-filled tubes, for which the load-carrying capacity of the tube wall is enhanced by the filler inside. Based on the symmetric fold's evolution process observed from numerical simulations, an analytical model is proposed to establish the expression of the tube wall's load-carrying capacity in relation to the internal pressure and the tube's size. It is shown that the tube wall's load-carrying capacity under higher internal pressure decreases with the internal pressure, while it increases with the cross-sectional area of the tube. By combining the analytical predictions obtained in the present paper under symmetric mode and that under non-symmetric mode reported in literature, the critical internal pressure for the transformation between the two deformation modes is estimated. All the analytical predictions are found to be in good agreements with the numerical simulation results.

© 2016 Elsevier Ltd. All rights reserved.

1. Introduction

As a classical kind of energy absorption components, tubes have been widely adopted in aircraft and vehicle structures. During the accidental impacts, they are crushed axially to absorb energy effectively while limiting the crushing force [1]. When the cylindrical tubes were axially compressed, four kinds of deformation modes are observed: ring mode (symmetric mode), diamond mode (non-symmetric mode), mixed mode and Euler buckling, as dictated by the tube's length and the ratio of the tube's diameter to its wall-thickness [2–4]. Alexander [5] first established an analytical model to predict the average crushing force of cylindrical tubes deforming with the ring mode. Then his work was modified in later references [6,7] to improve the accuracy. Bardi et al. [8] compared numerical crushing responses with those of the major plastic hinge models for the axisymmetric crushing mode. For the tubes deforming with diamond mode, the proposed analytical

models are not as successful as the ring mode due to the complex deformation process of the tube wall. Most of such models on the diamond mode involve the bending of the triangle elements around the plastic hinge lines. However, it is difficult to theoretically determine the number of the elements, which needs to be known in advance [9]. Thus, empirical formulas based on experiments are usually employed in predicting the tubes' average crush force [2].

Cellular materials have been proved to possess effective energy absorption capability [10–12], thus some researchers focused on the tubes filled with cellular materials inside. It is shown that the foam filler beneficially contributes in terms of failure modes, resulting in a much more stable crushing manner during axial compression tests [13]. Toksoy and Guden [14] carried out a series of experiments and found that the foam filling reduced the fold length and changed the deformation mode of the tube from multi-lobe mode to axisymmetric mode. Similar phenomena were observed in the wood-filled tubes [15]. Besides, Duarte [16] experimentally found that a good interface bonding between the tube and the filled foam contributed to a more axisymmetric deformation without distortion, while a lack of interface bonding resulted in an irregular fold with a certain distortion.

* Corresponding author at: Department of Applied Mechanics & Engineering, School of Engineering, Sun Yat-sen University, Guangzhou 510275, PR China.

E-mail addresses: huling@mail.sysu.edu.cn (L.L. Hu), llhu_80@163.com (Zh.H. Zeng).

Nomenclature

E	energy dissipated by tube wall
E_{DE}^b, E_{DE}^s	plastic bending energy and stretching energy, respectively, of arc DE
$\overline{E^b}, \overline{E^s}$	plastic bending energy and stretching energy, respectively, absorbed by the representative fold per unit displacement
F_{tw}	crushing force suffered by tube wall
F_p	force to balance internal pressure, $F_p = \pi R^2 p$
F_{total}	total compression force imposed by crushing plate
$F_{total} = F_{tw} + F_p$	
H_0, H_f	initial and final length of representative fold segment, respectively.

L	length of wall section
M_0	fully plastic bending moment per unit length of tube wall, $M_0 = \frac{\gamma t^2}{4}$
p_Y	yield pressure of tube
R	radius of tube
r_{center}	distance from centroid of area BDEF to tube's axis
r	radius of arc AB, see Fig. 8
t	thickness of tube wall
ΔV	lateral change in internal volume surrounded by fold segment during its evolution process
W_F	work done by crushing force
W_p	work done by internal pressure
Y	yield stress of tube wall material
$\alpha, \beta, \gamma, \delta, \zeta, \theta, \lambda, \varphi$	angle of each section, as shown in Fig. 8

Moreover, the mean crushing load and subsequently the specific energy absorption of the tubes were found to be enhanced by the filler [14,15]. The total crush force of the foam-filled tube can be divided into three parts, i.e., (1) the average crush force of non-filled tubes, (2) the uniaxial resistance of foam filler, and finally (3) an interaction effect [17]. Thus, the load-carrying capacity of the foam-filled tube is higher than the sum of that of the tube and the foam alone due to the interaction effect between the tube's inner wall and the foam filler [13,18].

The pulse buckling of water-filled cylindrical tubes under axial impact was experimentally and numerically investigated by Lu et al. [19], in which the water was sealed within the tube. Thus, quite high internal hydrodynamic pressure occurred inside the tube during the impact process, and the pressure rapidly increased with the crushing displacement. Under the combined action of high internal pressure and axial compression, the thin-walled tubes buckle plastically with regular and axisymmetric wrinkles. Another similar study by Paquette and Kyriakides [20] was conducted on the stainless-steel cylindrical tubes with pressurized fluid inside, in which the internal pressure was controlled as fixed values during the compression process. The experimental results showed that the internal pressure lowered the axial stress-strain response of the tubes. Besides, it was observed that all the pressurized cylinders developed axisymmetric wrinkling in contrast to the non-axisymmetric buckling modes for the tubes without internal pressure. It is noticed that all their experiments were only within small deflections (axial displacement < 5%). If the tubes are used for energy absorption devices, their behaviors under large plastic deformations need to be investigated.

Zhang and Yu [21] explored the possible use of air-pressurized thin-walled cylindrical tubes as adaptive energy absorbers and experimentally investigated those tubes' energy absorption behaviors under axial crushing with constant internal pressure. It was shown that with the increase of internal pressure the deformation mode of the tube changed from diamond mode with sharp corners to that with round corners, and finally to ring mode. In diamond mode, the tubes' mean force increased with internal pressure on account of two mechanisms: the direct effect of the internal pressure and the interaction between pressurized air and tube wall. The second mechanism became weaker after the deformation switched to ring mode. However, no reduced load-carrying capacity of the tubes caused by internal pressure was observed in their experiments, which was different from the reports of Paquette and Kyriakides [20]. It is noticed that the internal pressure in their studies [21] was limited in the range from 0% to 30% of the tube's yield pressure, and the tubes experienced large plastic deformation. On the other hand, the tubes' axial compression reported by Paquette and Kyriakides [20] was small although the internal pressure increased up to 75% of the tube's yield pressure. Thus, more work need to be done in a wide range of internal pressure to clarify the

effect of internal pressure on the force-displacement response of tubes axially crushed with large plastic deformation.

In the present paper, the crushing response of the pressurized thin-walled cylindrical tubes under axial impact was numerically investigated with the internal pressure varying in a wide range from 0% to 80% of the tube's yield pressure. Numerical simulations with lower internal pressure are verified by the experiments reported by Zhang and Yu [21]. Moreover, an analytical model is proposed to establish the dependence of the tube's load-carrying capacity on the internal pressure and the tube's own parameters.

2. Numerical simulations

2.1. Numerical model

Numerical simulations are carried out by employing the software ANSYS/LS-DYNA. A cylindrical tube without upper and bottom surfaces is put on a fixed rigid plate, and is axially crushed by another rigid plate from the top with a constant velocity $V=1$ m/s or $V=10$ m/s, as shown in Fig. 1. A constant air-pressure p is applied on the inner surface of the tube, which is always perpendicular to the tube's inner surface with a fixed magnitude during the whole crushing process. The internal pressure p is within the range from

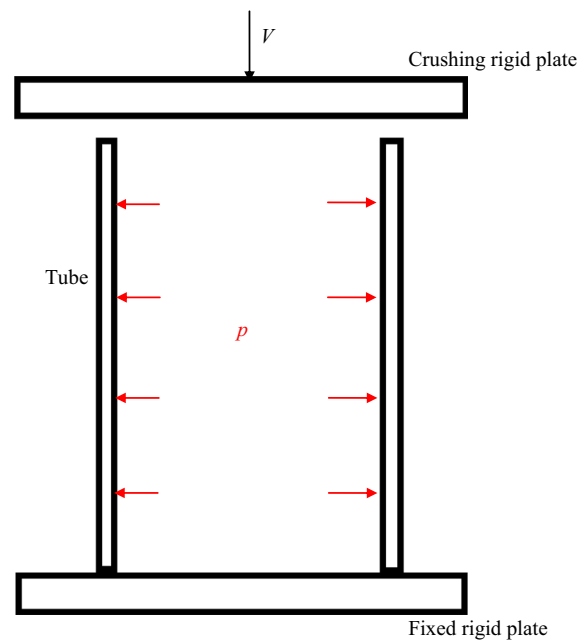


Fig. 1. Numerical model in simulations.

0% to 80% of the tube's yield pressure p_Y , which is defined as

$$p_Y = \frac{t}{R} Y \quad (1)$$

Two kinds of dimensions for the cylindrical tube are adopted in simulations. One is the same with that of the tube used in the experiments by Zhang and Yu [21] with length $H=150$ mm, radius $R=26.5$ mm and wall-thickness $t=0.21$ mm. The other is similar but $t=0.17$ mm. In experiments [21], the material of tube wall was mild steel. Tensile tests for the material were reported in Ref. [21], displaying a perfectly plastic behavior with Young's modulus $E=200$ GPa and yield stress $Y=380$ MPa. It is used for the material of tube wall in numerical simulations with Poisson's ratio $\mu=0.3$ and density 7800 kg/m³. The tube wall is meshed with the shell elements SHELL 163. Through the convergence study, it is found that 0.7 mm element size with five integration points along the shell thickness can provide accurate results, which results in 238 elements along the circumference and 214 elements along the length of the tube. Surface-to-surface contact is applied between the tube and the two rigid plates, whilst single surface contact is applied to the tube. The friction coefficient of all the contacts is set to be 0.1.

2.2. Experimental verification

In the crushing experiments reported by Zhang and Yu [21], the pressurized thin-walled cylindrical tubes were crushed by a drop hammer. The crushing velocity was less than 10 m/s and decreased

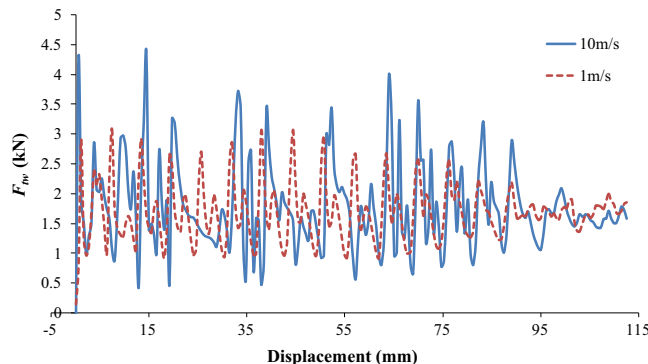


Fig. 2. Influence of crushing velocity on the tubes' crushing force.

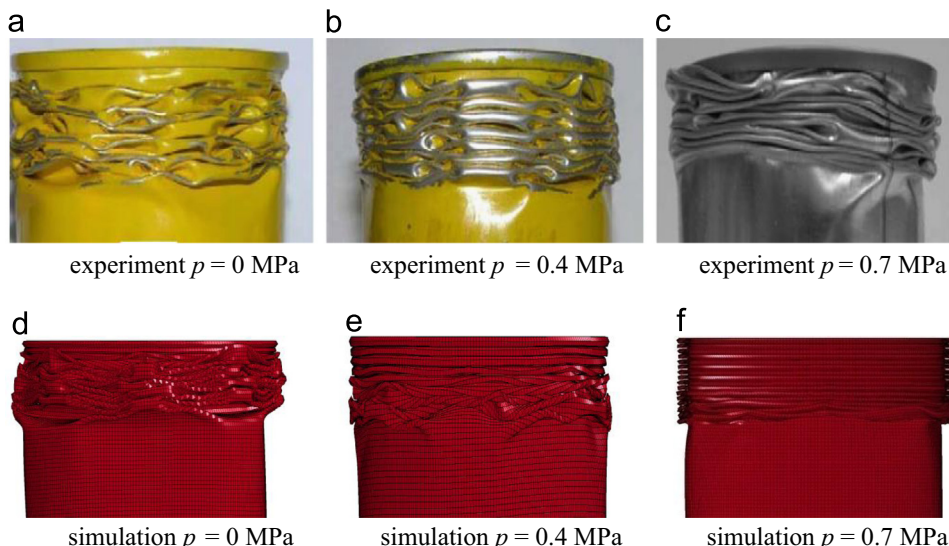


Fig. 3. Comparison of tubes' deformation between simulations and experiments ($t=0.21$ mm). (a) Experiment $p = 0$ MPa; (b) experiment $p = 0.4$ MPa; (c) experiment $p = 0.7$ MPa; (d) simulation $p = 0$ MPa; (e) simulation $p = 0.4$ MPa; and (f) simulation $p = 0.7$ MPa.

gradually during the crushing process. In our present study, to examine the influence of crushing velocity, two cases are simulated with constant crushing velocity of 1 m/s and 10 m/s, respectively. In both cases, the internal pressure remains as 1.6 MPa, and the wall-thickness of the tube is taken as $t=0.21$ mm. The impact forces suffered by the cylindrical tubes are compared for these two cases, as shown in Fig. 2, indicating that the tubes' impact force is almost not affected by the crushing velocity in the range of $V < 10$ m/s. Thus, considering the simulation efficiency, the constant crushing velocity of $V=10$ m/s is adopted in the following simulations.

The crushing experiments reported by Zhang and Yu [21] only employed the internal pressure less than 0.8 MPa, and the results were used to verify the numerical simulations. The tubes' deformations obtained by our numerical simulations are depicted in Fig. 3 to compare with the experimental results reported by Zhang and Yu [21]. The tubes' deformation seems more asymmetric in experiments. It is resulted by the defects in the cans, while no any defects are considered in the simulations. Nevertheless, both the experimental and the numerical results show that the tube without internal pressure deforms with the mixture of symmetric mode and non-symmetrical mode, as shown in Fig. 3(a) and (d). With the increase of internal pressure, the lobes' ridges of the non-symmetrical mode become rounder whilst the number of symmetric rings increases, as shown in Fig. 3(b) and (e). When the internal pressure increases to 0.7 MPa, the tube's deformation is dominated by the symmetric mode, i.e. the ring mode, as shown in Fig. 3(c) and (f).

The tubes are sealed on the upper and the bottom surfaces in the experiments reported by Zhang and Yu [21]. Thus, the total compression force imposed by the crushing plate F_{total} includes two parts, i.e., $F_{total}=F_{tw}+F_p$, where F_{tw} represents the crushing force suffered by the tube wall, and F_p is the force to balance the internal pressure. In numerical simulations, neither upper nor bottom surface exists for the tubes. By taking $F_p=\pi R^2 p$ into account, Fig. 4 compares the total compression force F_{total} of the numerical and experimental results, showing a good agreement with each other except the severer undulation in simulations resulted by ignoring the defects. Thus, our numerical simulations are verified by the experiments within the pressure range examined by Zhang and Yu [21]. In the following, we will pay more attention to the tube's behavior under higher internal pressure.

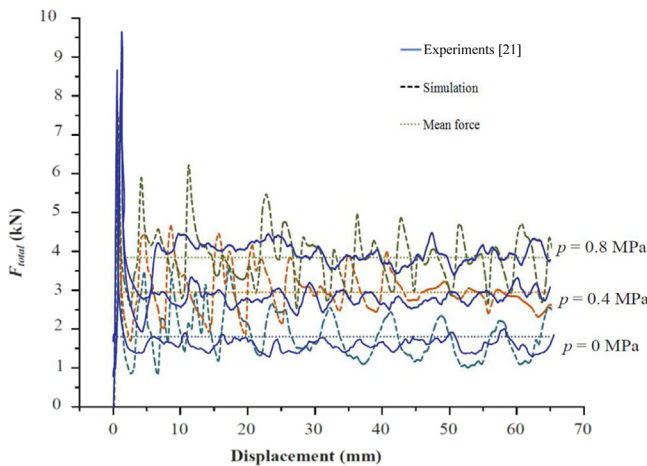


Fig. 4. Comparison of compression force between experiments [21] and simulations ($t=0.21$ mm).

2.3. Numerical results

In order to further study the effects of internal pressure on the mechanical behaviors of cylindrical tubes under axial crushing, numerical simulations are further carried out for the cases with higher internal pressures up to 80% of the tubes' yield pressure.

It is shown in Fig. 4 that the compression force F_{total} undulates around a certain value during the whole crushing process of the tube, except for the peak force, which appears at the initial instant of the crushing. In order to clearly exhibit the dependence of the crushing force on the internal pressure, the force in the following indicates the averaged value during the compression process. The average force (or called the mean crushing force) is one of the important indicators for the energy absorption capacity of the tubes.

Fig. 5 displays the effect of the internal pressure on both the mean crushing force suffered from by the tube wall, F_{tw} , and the total compression force $F_{total}=F_{tw}+F_p$. It is shown in Fig. 5(a) that the total compression force F_{total} increases with the internal pressure, indicating that the internal pressure can enhance the energy absorption capacity of the tubes, since extra work has to be done by the crushing plate to overcome the pressure inside the tube.

The dependence of the force applied on tube wall, F_{tw} , on the internal pressure, p , is displayed in Figs. 5(b) and (c). The vertical axis of Fig. 5(c) represents the increment of F_{tw} for the tubes with internal pressure, in excess of that without internal pressure. It is noted in Figs. 5(b) and (c) that the force applied on tube wall, F_{tw} , increases with the internal pressure when the internal pressure p is less than 0.4 MPa (13% of the yield pressure). The force applied on tube wall with internal pressure $p=0.4$ MPa is about 20% higher than that of the tube without internal pressure. However, once the internal pressure $p > 0.4$ MPa, F_{tw} decreases with the increase of p , even lower than that of the tube without internal pressure, e.g. for the cases of $p=2.0$ MPa and $p=2.4$ MPa. It is in agreement with the report on the small deformation of tubes with fluid inside [20], but is very different from the foam-filled tubes [14,17], for which the load-carrying capacity and the energy absorption capacity of the tubes are enhanced by the inside foam filler.

The variation of the tubes' load-carrying capacity with internal pressure, as shown in Fig. 5(b) and (c), is related to the tubes' deformation modes. The deformation modes of the tubes with various levels of internal pressure are exhibited in Fig. 6 with the tubes' crushing displacement being 100 mm for all the cases. The numbers of the deformation folds appeared in the deformed tubes are counted and listed in Table 1. Fig. 6 and Table 1 reveal that the tube's deformation is dominated by the non-symmetrical fold when the internal pressure is less than 0.4 MPa. In these cases, the number of the

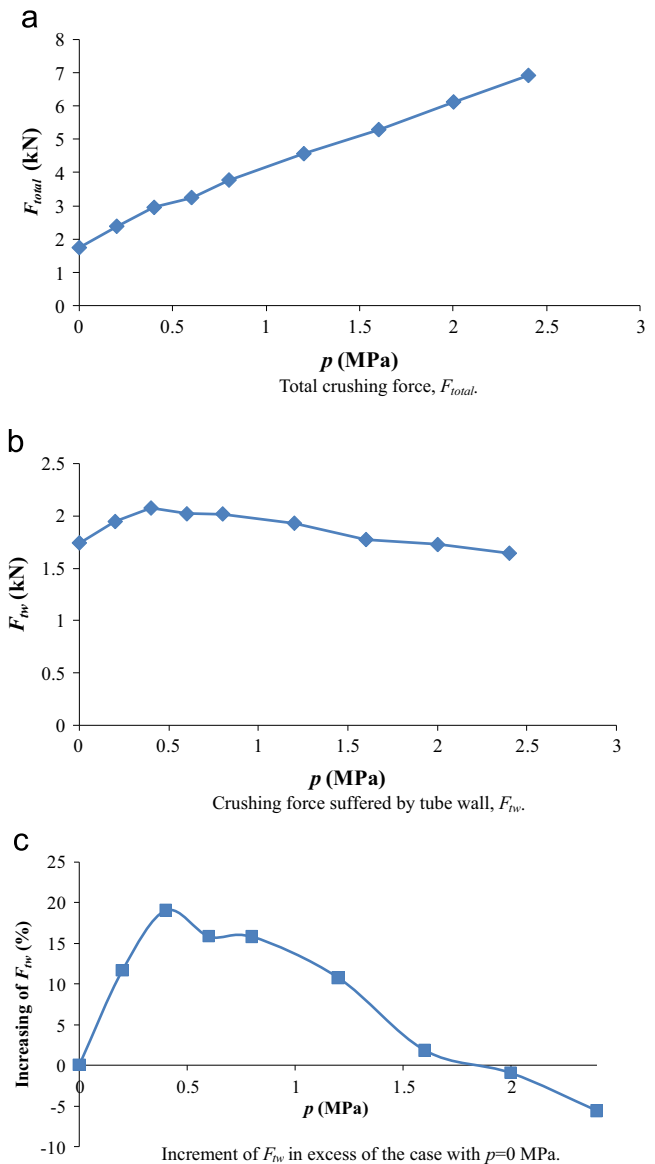


Fig. 5. Dependence of crushing force on the internal pressure ($t=0.21$ mm). (a) Total crushing force, F_{total} ; (b) crushing force suffered by tube wall, F_{tw} ; (c) increment of F_{tw} in excess of the case with $p=0$ MPa.

symmetric folds increases with the internal pressure, while the number of non-symmetrical folds remains unchanged until the internal pressure reaches to 0.4 MPa. Hence, the tube wall's load-carrying capacity F_{tw} increases with internal pressure when $p < 0.4$ MPa as shown in Fig. 5(b) and (c), since more symmetric folds dissipate more energy. Once the internal pressure $p > 0.4$ MPa, the number of non-symmetrical folds decreases rapidly and they are replaced by more symmetric folds; this is corresponding to the decrease of the tube's load-carrying capacity shown in Fig. 5(b) and (c). When the internal pressure increases to 1.2 MPa, only symmetric folds appear in the deformed tubes, and then the total number of the folds decreases with the increase of internal pressure, leading to the decrease of the tube's load-carrying capacity.

3. Theoretical analysis

A semi-empirical formula was presented by Zhang and Yu [21] to predict the mean crushing force of tubes deforming in non-

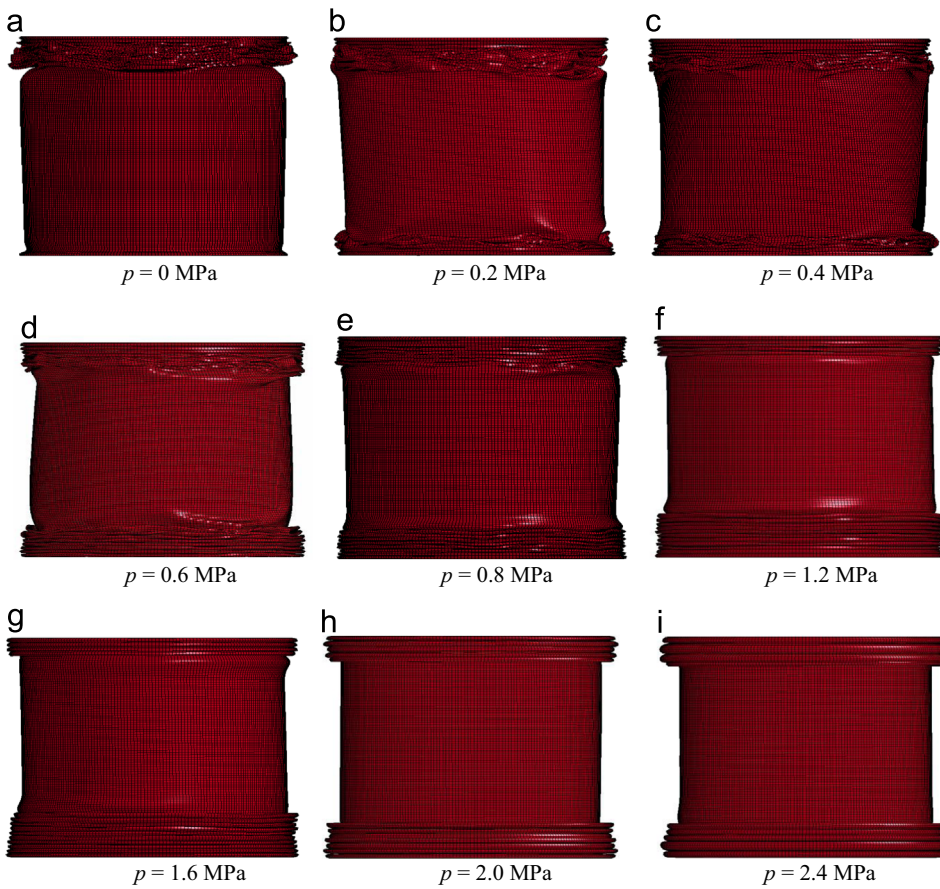


Fig. 6. Deformations of tubes with various internal pressures. (a) $p = 0$ MPa; (b) $p = 0.2$ MPa; (c) $p = 0.4$ MPa; (d) $p = 0.6$ MPa; (e) $p = 0.8$ MPa; (f) $p = 1.2$ MPa; (g) $p = 1.6$ MPa; (h) $p = 2.0$ MPa; and (i) $p = 2.4$ MPa.

Table 1
Deformation folds under various internal pressures.

Internal pressure (MPa)	Deformation folds
0	3 symmetric folds and 10 unsymmetrical folds
0.2	4 symmetric folds and 10 unsymmetrical folds
0.4	5 symmetric folds and 10 unsymmetrical folds
0.6	8 symmetric folds and 8 unsymmetrical folds
0.8	16 symmetric folds and 2 unsymmetrical folds
1.2	17 symmetric folds
1.6	14 symmetric folds
2.0	12 symmetric folds
2.4	9 symmetric folds

symmetric mode under lower internal pressures:

$$F_{total} = 2 \min \left(\frac{(1/2) \sum E_i - P \cdot \Delta V}{\delta_e \lambda} \right), \quad (2)$$

where

$$\sum E_i = M_0 \lambda \left\{ A_0 + A_1 \frac{R}{\lambda} + A_2 \frac{\lambda}{t} \right\}. \quad (3)$$

is the total energy dissipations, and

$$\Delta V \approx \frac{2N}{3} R^2 (\theta - \sin \theta \cos \theta) \sqrt{\lambda^2 - S^2} \quad (4)$$

is the lateral change in the internal volume surrounded by the fold segment during its evolution process. $\delta_e = 0.82$ is stroke coefficient, and λ is the arc length of a half fold. M_0 is the plastic limits of bending moment. N is the number of lobes along the circumferential direction. For $N=4$ and 5, the coefficients A_0 , A_1 , and A_2 are 94.8, 26.3, 3.0 and 140.5, 26.3, 4.72, respectively. θ is the half

central angles of a single straight section along the circumference, and S is the horizontal span of a layer of fold.

For the tubes deforming in symmetric mode under higher internal pressure, in the following we propose an analytical model so as to predict the tube's load-carrying capacity and its dependence on the internal pressure applied.

3.1. Evolution of fold

The evolution process of a typical symmetric fold is carefully tracked in numerical simulations. The evolution of an axial profile of the typical fold is exhibited in Fig. 7, indicating that the fold's profile consists of several sections as marked by ABCDEFG. At the initial instant of the fold's formation, all the sections are straight lines and lie along the undeformed tube wall, as shown in Fig. 7(a). With the compression of the tube, section DE bends outward as a curve, while sections CD and EF almost remain as straight lines but become inclined due to the bending of section DE, as shown in Fig. 7(b). At the same time, sections AC and FG also bend to curves while remain smooth connections with the neighbor sections. Once sections CD and EF approach respective horizontal positions, as shown in Fig. 7(c), with further compression of the tube, line CD rotates around point D with sections DE, EF and FG almost holding standstill until curve AC contacts with section FG at points B and F, as shown in Figs. 7(d) and (e). By then, a period of the fold's evolution process is completed; meanwhile the next fold begins to form and evolve.

An idealized model as shown in Fig. 8 is proposed to describe the evolution process of a typical fold. At the initial instant, all the sections within the fold lie along the undeformed tube wall. With the compression of the tube, as shown in Fig. 8(a), sections A'C, DE and FG bend to arcs with AA' still lying along the undeformed tube

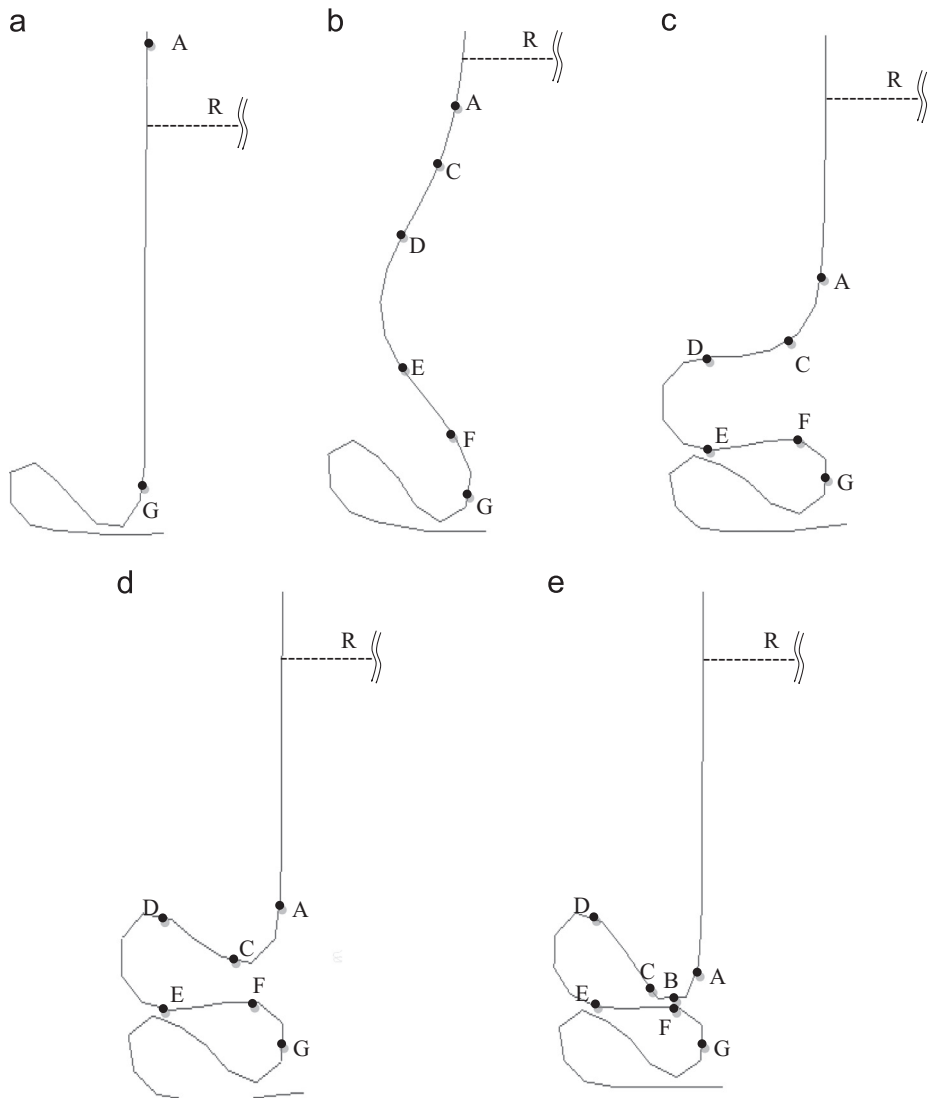


Fig. 7. Evolution process of the typical fold in numerical simulations.

wall. Line EF is assumed to be always tangential to arcs DE and FG at points E and F, respectively, while line CD is always tangential to curves A'C and DE at points C and D, respectively, until lines CD and EF rotate to the respective horizontal positions, as shown in Fig. 8(b), which corresponds to Fig. 7(c). At the instant as shown in Fig. 8(b), section DE is idealized as a semi-circle, while sections A'C and FG are idealized as quarter circles. The radius of arcs A'C, DE, and FG are assumed to be the same, r . Thus, the lengths of lines CD and EF are equal to each other, i.e.,

$$L_{CD} = L_{EF}, \quad (5)$$

where L_{CD} and L_{EF} are the length of lines CD and EF, respectively.

Then with further compression of the tube, sections DE, EF and FG hold standstill. Line CD rotates about point D while remaining the tangential connection with arc A'C at point C, until curve ABC contacts with arc FG at points B and F, indicating the final instant of the fold's evolution period, as shown in Fig. 8(c). At the final instant shown in Fig. 8(c), arc AB is a quarter circle with radius r . The angle of arc BC is α . Thus, the inclined angle of line CD to the horizontal direction is also equal to α on account of the tangential connection between line CD and arc BC. Since arc BC is much shorter compared to the length of line CD, straight line BD is used to replace sections CD and BC to simplify the calculation in geometry, as shown in Fig. 8(c). Then the value of α is approximately

calculated as

$$\alpha = \arctg \frac{2r}{L_{EF}}. \quad (6)$$

3.2. Load-carrying capacity of tube

Since the tube is made of perfectly plastic material in both experiments [21] and numerical simulations, rigid, perfectly plastic material with yield stress Y is considered for the tube wall in the theoretical analysis. It is also assumed that the bending and the stretching of the tube wall have no interactions in the yield criterion. The change in the wall's length along the tube's axial direction is ignored. The tube wall suffers from the crushing force, F_{tw} , and the internal pressure, p . The work done by them is dissipated by the plastic deformation of the tube wall during the folds' evolution process. By focusing on the representative fold segment ABCDEFG, as shown in Fig. 8, the energy relationship is

$$W_F + W_p = E_{tw} = E_{AC} + E_{CD} + E_{DE} + E_{EF} + E_{FG}, \quad (7)$$

where W_F and W_p are the work done by the crushing force, F_{tw} , and the internal pressure, p , respectively, during the evolution process of the fold. E_{tw} denotes the total energy absorbed by the

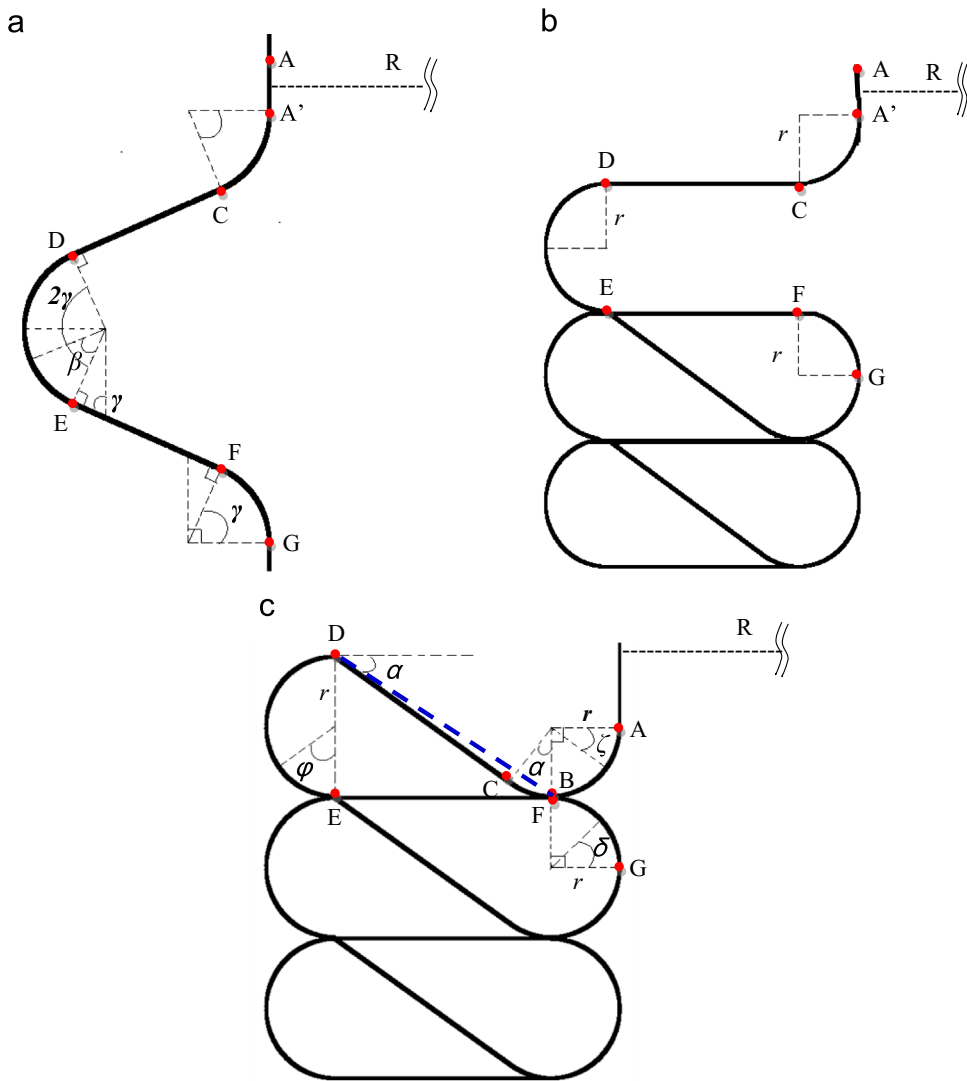


Fig. 8. Idealized model for the evolution process of the typical fold.

tube wall; E_{AC} , E_{CD} , E_{DE} , E_{EF} and E_{FG} denote the energy dissipated by sections AC, CD, DE, EF and FG, respectively.

The initial length of the representative fold segment, H_0 , is

$$H_0 = L_{CD} + L_{EF} + (2\pi + \alpha)r, \quad (8)$$

and the final length, H_f , is

$$H_f = 2r + 2t. \quad (9)$$

Thus, the work done by the crushing force during an evolution period of a symmetric fold is obtained as

$$W_F = F_{tw}(H_0 - H_f). \quad (10)$$

The internal pressure is always perpendicular to the tube's wall. The work done by the internal pressure to the tube, W_p , can be expressed by

$$W_p = P \cdot \Delta V, \quad (11)$$

where ΔV is the lateral change in the internal volume surrounded by the fold segment during its evolution process. It can be calculated by referring to Fig. 8(c),

$$\Delta V = \left(\frac{\pi r^2}{2} + rL_{EF} \right) \cdot 2\pi R_{center}, \quad (12)$$

where $\left(\frac{\pi r^2}{2} + rL_{EF} \right)$ is the area surrounded by sections BD, DE and EF at the final instant of the fold's evolution process, see Fig. 8(c);

R_{center} is the distance from the center of area BDEF to the tube's axis, written as

$$R_{center} = \frac{\left[\left(\frac{2L_{EF}}{3} + R + r \right) \cdot \frac{L_{EF}}{2} \cdot 2r + \left(R + r + L_{EF} + \frac{4r}{3\pi} \right) \cdot \frac{\pi r^2}{2} \right]}{\left(\frac{\pi r^2}{2} + rL_{EF} \right)} \\ = R + r + \frac{4L_{EF}^2 + 3\pi L_{EF}r + 4r^2}{3\pi r + 6L_{EF}}. \quad (13)$$

By submitting Eqs. (12) and (13) into Eq. (11), the work done by the internal pressure to the tube, W_p , is written as:

$$W_p = p \cdot \Delta V = \frac{1}{3}\pi p R^2 t \frac{R}{tR} \left[4 \left(\frac{L_{EF}}{R} \right)^2 + 6 \left(\frac{L_{EF}}{R} \right) + (6 + 3\pi) \frac{L_{EF} r}{R} \right. \\ \left. + 3\pi \frac{r}{R} + (4 + 3\pi) \left(\frac{r}{R} \right)^2 \right]. \quad (14)$$

Arches AC and FG shown in Fig. 8(c) are bent from the straight wall with the energy dissipated by both the plastic bending and the stretching of the tube wall along the circumference. The latter is resulted from the enlargement of the sections displaced from the tube's axis. Thus, the energy dissipations by sections AC and FG are

$$E_{AC} = \int_0^{\frac{\pi}{2} + \alpha} 2\pi(R + r - r \cos \zeta) M_0 d\zeta$$

$$+Yt\left[\int_0^{\frac{\pi}{2}+\alpha} 2\pi(R+r-r \cos \zeta)rd\zeta-2\pi Rr\left(\frac{\pi}{2}+\alpha\right)\right] \\ =\pi YR^2 t\left\{\left[\frac{1}{4R}\left(1+\frac{r}{R}\right)+\left(\frac{r}{R}\right)^2\right]\left[\pi+2\arctan\left(\frac{2\frac{r}{R}}{\frac{L_{EF}}{R}}\right)\right]-\frac{\frac{r}{R}\frac{L_{EF}}{R}\left[\frac{L_{EF}}{R}+4\frac{r}{R}\right]}{2\sqrt{\left(\frac{L_{EF}}{R}\right)^2+4\left(\frac{r}{R}\right)^2}}\right\} \quad (15)$$

and

$$E_{FG}=\int_0^{\frac{\pi}{2}} 2\pi(R+r-r \cos \delta)M_0 d\delta \\ +Yt\left[\int_0^{\frac{\pi}{2}} 2\pi(R+r-r \cos \delta)rd\delta-\pi^2 Rr\right] \\ =\pi YR^2 t\left[\frac{\pi t}{4R}\left(1+\frac{r}{R}\right)-\frac{1}{2}\frac{r t}{R R}+(\pi-2)\left(\frac{r}{R}\right)^2\right], \quad (16)$$

respectively, where $M_0=\frac{Yt^2}{4}$ is the fully plastic bending moment per unit length of the tube wall.

The straight line EF in Fig. 8(c) comes from the directly falling down of the vertical tube wall while it always remains tangential to arcs DE and FG, thus only the stretching energy of the tube wall need to be considered for the energy dissipated by section EF, i.e.,

$$E_{EF}=[\pi(R+r+L_{EF})^2-\pi(R+r)^2-2\pi RL_{EF}] \cdot Yt=\pi YR^2 t \frac{L_{EF}}{R}\left(\frac{L_{EF}}{R}+2\frac{r}{R}\right). \quad (17)$$

As for line CD, besides the stretching energy of the tube wall, a plastic hinge at point D will also dissipate energy. Thus, the energy dissipated by section CD during the fold's evolution process, E_{CD} , is

$$E_{CD}=[\pi(R+r+r \sin \alpha+R+r+L_{EF})L_{CD}-2\pi RL_{CD}]Yt \\ +2\pi(R+r+L_{EF})M_0 a \\ =\pi YR^2 t\left[\left(2\frac{r}{R}\frac{L_{EF}}{R}+\frac{2}{\sqrt{\left(\frac{L_{EF}}{R}\right)^2+4\left(\frac{r}{R}\right)^2}}\frac{L_{EF}}{R}\frac{r^2}{R R^2}+\frac{L_{EF}^2}{R^2}\right) \right. \\ \left.+\frac{t}{2R}\left(1+\frac{r}{R}+\frac{L_{EF}}{R}\right)\arctan\left(\frac{2\frac{r}{R}}{\frac{L_{EF}}{R}}\right)\right]. \quad (18)$$

During the evolution process of arc DE, the energy is dissipated by both the plastic bending of the tube wall and the wall's stretching along the circumference. According to Fig. 8(a), the plastic bending energy of arc DE, E_{DE}^b , is

$$E_{DE}^b=\int_0^{\frac{\pi}{2}} \int_0^{2\gamma} 2\pi\left[R+\frac{\pi r}{2\gamma}-\frac{\pi r}{2\gamma} \cos \gamma+L_{EF} \sin \gamma+\frac{\pi r}{2\gamma} \cos (\gamma-\beta)-\frac{\pi r}{2\gamma} \cos \gamma\right] \cdot M_0 d\beta d\gamma. \quad (19)$$

The wall's stretching energy along the circumference, E_{DE}^s , can be calculated based on the final state of the deformed fold as shown in Fig. 8(c),

$$E_{DE}^s=2\pi Yrt[\int_0^{\pi}(R+r+L_{EF}+r \sin \varphi)d\varphi-\pi R]. \quad (20)$$

Hence, the total energy dissipated by arc DE during the evolution process of the fold, E_{DE} , is given by

$$E_{DE}=E_{DE}^b+E_{DE}^s=2\pi YR^2 t\left[\int_0^{\frac{\pi}{2}} \frac{t}{4R}\left(2\gamma+\frac{\pi r}{R}-2\pi \frac{r}{R} \cos \gamma+2\gamma \frac{L_{EF}}{R} \sin \gamma\right.\right. \\ \left.\left.+\pi \frac{r \sin \gamma}{R}\right)d\gamma+\frac{r}{R}\left(\pi \frac{r}{R}+\pi \frac{L_{EF}}{R}+2\frac{r}{R}\right)\right] \quad (21)$$

By submitting Eqs. (8)–(11) into Eq. (7), the crushing force suffered by the tube wall is expressed as:

$$F_{tw}=\frac{E_{AC}+E_{CD}+E_{DE}+E_{EF}+E_{FG}-P \cdot \Delta V}{R\left\{2\frac{L_{EF}}{R}+\frac{r}{R}\left[2\pi-2+\arctan\left(\frac{2\frac{r}{R}}{\frac{L_{EF}}{R}}\right)\right]-2\frac{r}{R}\right\}}. \quad (22)$$

By substituting the expressions of each item, i.e., Eqs. (14)–(18) and (21), into the numerator of Eq. (22), it is found that Eq. (22) is essentially a function of $\frac{L_{EF}}{R}$ and $\frac{r}{R}$. These two unknowns can be determined by the minimization of the force, i.e.,

$$\begin{cases} \frac{\partial F_{tw}}{\partial\left(\frac{L_{EF}}{R}\right)}=0 \\ \frac{\partial F_{tw}}{\partial\left(\frac{r}{R}\right)}=0 \end{cases}. \quad (23)$$

Then by substituting the values of $\frac{L_{EF}}{R}$ and $\frac{r}{R}$ which are obtained from Eq. (23), into Eqs. (14)–(18) and (21), the crushing force suffered by the tube wall, F_{tw} , can be finally obtained according to Eq. (22). The analytical predictions on F_{tw} obtained from Eq. (22) are compared with the numerical results as shown in Fig. 9, revealing a good agreement between them.

Eq. (22) is workable for the tubes deforming with symmetric mode similar to Figs. 7 and 8, which is much easier to occur for the thick-wall tubes. Thus the analytical predictions are applicable for both thin-wall and thick-wall tubes. Based on Eq. (22), the variety of F_{tw} with both the wall-thickness ratio, R/t , and the normalized internal pressure, p/p_y , is shown in Fig. 10, in which the tube's radius is $R=26.5$ mm. It is shown that the load-carrying capacity of the tube wall decreases with the increase of both R/t and p/p_y .

Besides, it is noted that each item in the numerator of Eq. (22) is proportional to $R^2 t$, while the items in the denominator are proportional to R . Thus when t/R is constant, the crushing force suffered by the tube wall, F_{tw} , is proportional to Rt , i.e., F_{tw} linearly increases with both the tube's radius, R , and the thickness of tube wall, t . In other words, F_{tw} is proportional to the cross-sectional area of the tube.

4. Discussion

4.1. Energy partitioning

In a period of a symmetric fold's evolution process, the total energy absorbed by the tube wall, E_{tw} , can be calculated based on Eqs. (7), (15)–(18) and (21), then divided by the reduction of the fold ($H_f - H_0$), producing the energy absorbed by the tube wall per unit displacement $\bar{E}_{tw}=E_{tw}/(H_f - H_0)$, and the variation of \bar{E}_{tw} with the internal pressure is exhibited as the solid curve in Fig. 11. It is shown that the total energy absorbed by the tube wall per unit displacement is not notably affected by the internal pressure, which can be verified by the numerical simulations, as shown in Fig. 12. Fig. 12 displays the energy absorbed by the tube wall during the numerical compression process under various internal pressures. It is shown that all the curves coincide together,

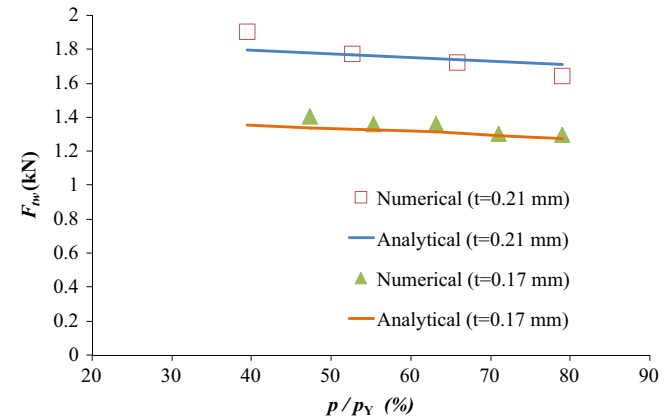


Fig. 9. Comparison of F_{tw} between analytical predictions and numerical results.

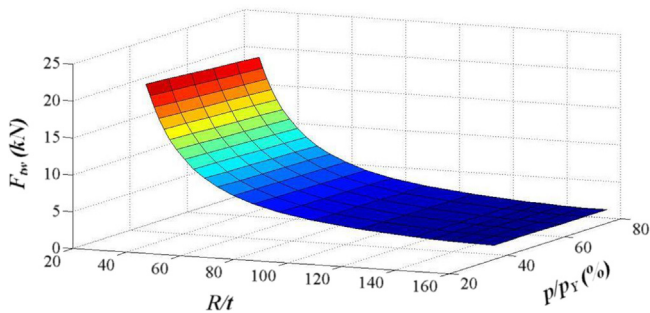


Fig. 10. Variety of F_{tw} with both wall-thickness ratio, R/t , and normalized internal pressure, p/p_Y ($R=26.5$ mm).

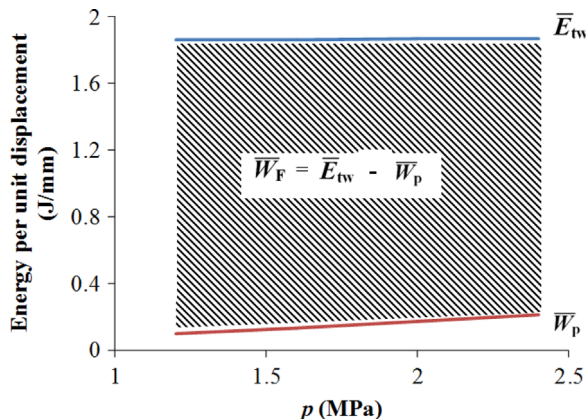


Fig. 11. Map of energy partition ($t=0.21$ mm).

indicating the little influence of the internal pressure on the total energy absorbed by the tube wall.

The dependence of both the bending energy, \bar{E}^b , and the stretching energy, \bar{E}^s , absorbed by the fold per unit displacement on the internal pressure, p , is respectively plotted in Fig. 13 based on the analytical formulas. It is shown that the bending energy, \bar{E}^b , decreases with the inner pressure, while the stretching energy, \bar{E}^s , increasing. Recalling the tubes' deformation mode observed in numerical simulations with $p > 1.2$ MPa, as shown in Fig. 6 and summarized in Table 1, with the increase of internal pressure, the total number of symmetric folds decreases, resulting in less bending energy being dissipated by the tube wall. However, in the same time, the total length of the folds increases with the internal pressure since it is inversely proportional to the folds' number. Thus, more stretching energy has to be dissipated by the more serious expansion of the tube wall along the circumferential direction. The increased stretching energy is counteracted by the decreased bending energy, leading to almost no change in the total energy absorbed by the tube wall under various internal pressures.

The work done by the internal pressure per unit displacement in a period of the fold's evolution process, $\bar{W}_p = W_p/(H_f - H_0)$, can be calculated by Eqs. (8), (9) and (14), and its dependence on the internal pressure is plotted as the dotted curve in Fig. 11. It is shown that high internal pressure does more work when the tube deforms. Since $W_F = E_{tw} - \bar{W}_p$ with E_{tw} almost being unchanged, the work done by the crushing force per unit displacement, \bar{W}_F , decreases with the increase of internal pressure, as shown with the shadow portion in Fig. 11.

4.2. Transition from non-symmetric mode to symmetric mode

For the tubes deforming in non-symmetric mode, a semi-empirical formula was proposed by Zhang and Yu [21] to predict the dependence of the tube's mean crushing force on the internal

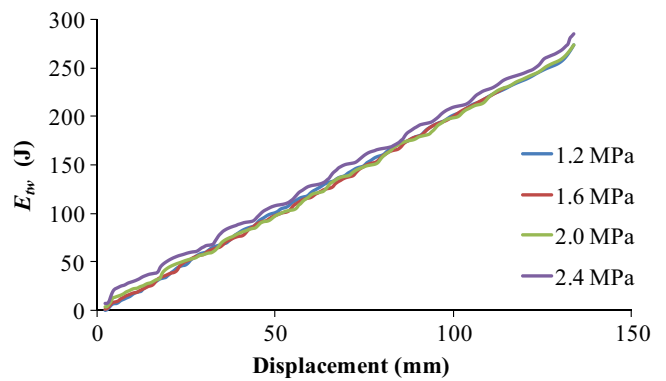


Fig. 12. Absorbed energy by tubes with various internal pressure in numerical simulations ($t=0.21$ mm).

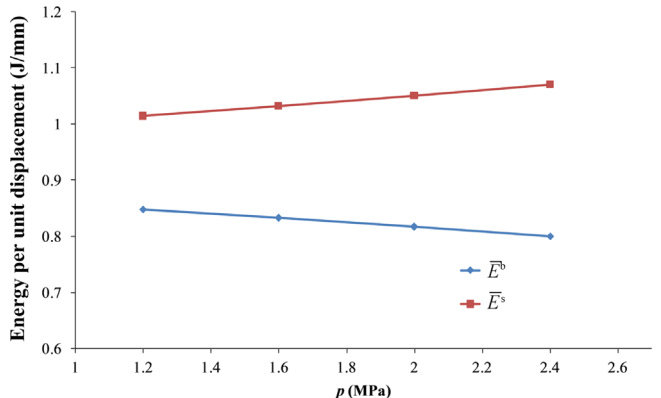


Fig. 13. Dependence of bending energy and stretching energy on internal pressure.

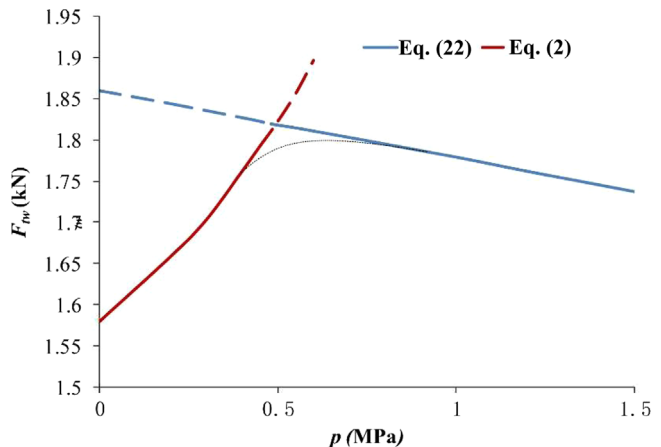


Fig. 14. Predictions on the tube wall's mean crushing force.

pressures, which is plotted in Fig. 14 in contrast to the predictions on that deforming in symmetric mode deduced in the present paper, i.e., Eq. (22). It is shown that the load-carrying capacity of the tube wall, F_{tw} , increases with the internal pressure in the theory under non-symmetric mode, while it decreases with the internal pressure under symmetric mode. The two analytical curves intersect at $p=0.48$ MPa, indicating the transformation between the two deformation modes. When $p < 0.48$ MPa, the non-symmetric model represented by Eq. (3) is applicable, while the symmetric model expressed by Eq. (22) is effective when $p > 0.48$ MPa, as shown with the solid branch of each curve in Fig. 14.

Recalling the tubes' deformation mode observed in numerical simulations as summarized in Table 1, it is shown that at

$p=0.6$ MPa the number of symmetric folds and that of the non-symmetric folds are about to be equal to each other, and this pressure magnitude is slightly higher than the analytical prediction of $p=0.48$ MPa. However, this is qualitatively understandable by noting the fact that both the two modes synchronously appear on the tube within the range $p \leq 0.8$ MPa, as shown in Table 1. By considering the actual gradual transition between the two modes, the two “theoretical” curves plotted in Fig. 14 should be connected with an arc tangential to both of them, as the dotted curve in the figure. Since the curve’s slope of the non-symmetric mode is steeper than that of the symmetric mode, the peak point of the mode transition curve will slightly move to the right compared with the intersection of the two theoretical curves at $p=0.48$ MPa, i.e., more close to the point of $p=0.6$ MPa as observed in the numerical simulation.

5. Conclusion

The novelty of the present study is at revealing how the deformation modes and the axial load-carrying capacity of pressurized tubes vary with the internal pressure. It is shown that the tube with lower internal pressure deforms with mixture of symmetric mode and non-symmetrical mode. With the increase of internal pressure, the tube’s deformation is dominated by the symmetric mode. The total load-carrying capacity of the pressurized tube increases with the internal pressure, since extra work has to be done by the crushing plate to overcome the internal pressure of the tube. However, if focus on the load carried by the tube wall alone, it is interesting to reveal that the internal pressure can enhance the tube wall’s load-carrying capacity when the wrinkles of the deformed tube are dominated by non-symmetric mode, while the tube wall’s load-carrying capacity decreases with the increase of the internal pressure once the symmetric mode dominates the deformed tube under the internal pressure greater than 13% of the yield pressure. It also gives an explanation on the different results reported in literatures [20,21] about the effect of the internal pressure on the tubes’ mechanical response.

Based on the evolution process of a typical symmetric fold in the tube observed in numerical simulations under higher internal pressure, an analytical model is established to predict the tube wall’s load-carrying capacity as a function of the internal pressure and the tube’s size. The analytical predictions are found to be in good agreement with the numerical results. Both the analytical predictions and the numerical simulations show that the load-carrying capacity of the tube wall decreases with the internal pressure, while increases with both the tube’s wall thickness and radius.

It should be emphasized that the total energy absorbed by the tube is almost independent from the internal pressure, although the tube’s load-carrying capacity decreases with the increase of the internal pressure, which is attributed to the increasing work of the increasing internal pressure done to the deformed tube. Moreover, by combining the analytical predictions obtained in the present paper under symmetric mode and that under non-

symmetric mode reported by Zhang and Yu [21], the critical internal pressure for the transformation between the two deformation modes is estimated.

Acknowledgments

The authors would like to thank the support from the National Natural Science Foundation of China under Grant nos.11172335 and 11472314, and the support from the opening project of State Key Laboratory of Explosion Science and Technology (Beijing Institute of Technology) No. KFJJ14-4M.

References

- [1] Lu G, Yu TX. Energy absorption of materials and structures. Cambridge: Woodhead Pub; 2001.
- [2] Guillow SR, Lu G, Grzebieta RH. Quasi-static axial compression of thin-walled. *Int.J. Mech. Sci.* 2001;43:2103–23.
- [3] Alghamdi AAA. Collapsible impact energy absorbers: an overview. *Thin-Walled Struct.* 2001;39:189–213.
- [4] Tvergaard V. On the transition from a diamond mode to an axisymmetric mode of collapse in cylindrical shells. *Int. J. Solids Struct.* 1983;19:845–56.
- [5] Alexander JM. An approximate analysis of the collapse of thin cylindrical shells under axial loading. *Q. J. Mech. Appl. Math.* 1960;13:11–5.
- [6] Singace AA, Elsobky H, Reddy TY. On the eccentricity factor in the progressive crushing of tubes. *Int. J. Solids Struct.* 1995;32:3589–602.
- [7] Wierzbicki T, Bhat SU, Abramowicz W, Brodkin D. Alexander revisited – a two folding elements model of progressive crushing of tubes. *Int. J. Solid Struct.* 1992;29:3269–88.
- [8] Bardi FC, Yun HD, Kyriakides S. On the axisymmetric progressive crushing of circular tubes under axial compression. *Int. J. Solids Struct.* 2003;40:3137–55.
- [9] Singace AA. Axial crushing analysis of tubes deforming in the multi-lobe mode. *Int. J. Mech. Sci.* 1999;41:865–90.
- [10] Hu LL, Yu TX. Mechanical behavior of hexagonal honeycombs under low-velocity impact theory and simulations. *Int. J. Solids Struct.* 2013;50:3152–65.
- [11] Gibson LJ, Ashby MF. Cellular solids structure and properties. 2nd ed. Cambridge University Press; 1997.
- [12] Hu LL, Liu Y. Dynamic response of the gradient foams. *Strength Mater.* 2014;46(2):172–7.
- [13] Duarte I, Krstulovic'-Opara L, Vesenjak M. Characterisation of aluminium alloy tubes filled with aluminium alloy integral-skin foam under axial compressive loads. *Compos. Struct.* 2015;121:154–62.
- [14] Toksoy AK, Guden M. The strengthening effect of polystyrene foam filling in aluminum thin-walled cylindrical tubes. *Thin-Walled Struct.* 2005;43:333–50.
- [15] Singace AA. Collapse behaviour of plastic tubes filled with wood sawdust. *Thin-Walled Struct.* 2000;37:163–87.
- [16] Duarte I, Vesenjak M, Krstulovic'-Opara L, Ren Z. Static and dynamic axial crush performance of in-situ foam-filled tubes. *Compos. Struct.* 2015;124:128–39.
- [17] Hanssen AG, Langseth M, Hopperstad OS. Static and dynamic crushing of circular aluminium extrusions with aluminium foam filler. *Int. J. Impact Eng.* 2000;24:475–507.
- [18] Zheng G, Wu SZH, Sun GY, Li GY, Li Q. Crushing analysis of foam-filled single and bitubal polygonal thin-walled tubes. *Int. J. Mech. Sci.* 2014;87:226–40.
- [19] Lu GY, Han ZJ, Lei JP, Zhang SY. A study on the impact response of liquid-filled cylindrical shells. *Thin-Walled Struct.* 2009;47:1557–66.
- [20] Paquette JA, Kyriakides S. Plastic buckling of tubes under axial compression and internal pressure. *Int. J. Mech. Sci.* 2006;48:855–67.
- [21] Zhang XW, Yu TX. Energy absorption of pressurized thin-walled circular tubes under axial crushing. *Int. J. Mech. Sci.* 2009;51:335–49.